A Computer-Driven Scaffold-Hopping Approach Generating New PTP1B Inhibitors from the Pyrrolo[1,2-a]quinoxaline Core

Javier García-Marín,*[a, b, f, g] Mercedes Griera,[c, e] Ramón Alajarín,[a, b, f] Manuel Rodríguez-Puyol,[b, e] Diego Rodríguez-Puyol,[b, d] and Juan J. Vaquero*[a, b, f]

Protein tyrosine phosphatase 1B (PTP1B) is a very promising target for the treatment of metabolic disorders such as type II diabetes mellitus. Although it was validated as a promising target for this disease more than 30 years ago, as yet there is no drug in advanced clinical trials, and its biochemical mechanism and functions are still being studied. In the present study, based on our experience generating PTP1B inhibitors, we have developed and implemented a scaffold-hopping approach to vary the pyrrole ring of the pyrrolo[1,2-a]quinoxaline core, supported by extensive computational techniques aimed to explain the molecular interaction with PTP1B. Using a combination of docking, molecular dynamics and end-point free-energy calculations, we have rationally designed a hypothesis for new PTP1B inhibitors, supporting their recognition mechanism at a molecular level. After the design phase, we were able to easily synthesize proposed candidates and their evaluation against PTP1B was found to be in good concordance with our predictions. Moreover, the best candidates exhibited glucose uptake increments in cellulo model, thus confirming their utility for PTP1B inhibition and validating this approach for inhibitors design and molecules thus obtained.

Introduction

Reversible protein phosphorylation is a key step in cellular and biochemical homeostasis, controlling signaling propagation inside the cell. All intracellular signaling cascades are tuned by a fine balance in the degree of protein phosphorylation, which is carried out by protein kinases. In this regard, protein phosphate groups are removed by the action of protein phosphatases. As such, alterations or aberrant changes in the activity of both types of proteins are linked to abnormalities such as cancer or immunological disorders, which is why some of them are considered very important therapeutic targets for drug development.[1] As an example, a considerable number of clinically approved inhibitory drugs, especially in oncology are molecules target kinases.[2] However, despite their potential to treat some diseases, protein phosphatases currently remain "undruggable", therefore research in the field of phosphatase inhibition and mechanistic studies is of great interest for the scientific community.[3–5] I this regard, a phosphatase described by Tonks et al. in 1988 has attracted the interest and attention of the scientific community for decades, especially in the drug discovery field.[6–9]

Protein tyrosine phosphatase 1B (PTP1B), an enzyme which catalyzes dephosphorylation of phosphotyrosine (pTyr) residues insulin receptor, and related substrates, via a two-step mechanism that is shared among protein phosphatases, is an archetypical phosphatase.[10] PTP1B is a negative regulator of insulin signal transduction and it regulates leptin signaling.[11] Additionally, this enzyme has been validated as a promising target for the treatment of type 2 diabetes mellitus.[12]

[a] Dr. J. García-Marín, Dr. R. Alajarín, Prof. J. J. Vaquero
Departamento de Química Orgánica y Química Inorgánica,
Universidad de Alcalá
28805 Alcalá de Henares (Spain)
E-mail: javier.garciamarin@uah.es
juanjose.vaquero@uah.es

[b] Dr. J. García-Marín, Dr. R. Alajarín, Prof. M. Rodríguez-Puyol,
Dr. D. Rodríguez-Puyol, Prof. J. J. Vaquero
Instituto Ramón y Cajal de Investigación Sanitaria (IRYCIS)
Ctra. Colmenar Viejo, km. 9100
28034 Madrid (Spain)

[c] M. Griera
Graphenano Medical Care, S.L.
C/Pablo Casals, no. 13, Yecla, Murcia (Spain)

[d] Dr. D. Rodríguez-Puyol
Fundación de Investigación Biomédica,
Unidad de Nefrología del Hospital Príncipe de Asturias y
Departamento de Medicina y Especialidades Médicas,
Universidad de Alcalá
28805 Alcalá de Henares (Spain)

[e] M. Griera, Prof. M. Rodríguez-Puyol
Departamento de Biología de Sistemas,
Universidad de Alcalá
28805 Alcalá de Henares (Spain)

[f] Dr. J. García-Marín, Dr. R. Alajarín, Prof. J. J. Vaquero
Instituto de Investigación Química Andrés Manuel del Río (IQAR),
Universidad de Alcalá, Alcalá de Henares (Spain)

[g] Dr. J. García-Marín
Departamento de Química Biológica y Estructural,
Centro de Investigaciones Biológicas Margarita Salas (CIB-CSIC)
Calle Ramiro de Maeztu 9
28040 Madrid (Spain)

Supporting information for this article is available on the WWW under https://doi.org/10.1002/cmdc.202100338

ChemMedChem

Full Papers
doi.org/10.1002/cmdc.202100338

**Chemistry
Europe**
European Chemical
Societies Publishing

Furthermore, PTP1B has been linked to other important diseases such as breast cancer, metabolic syndrome, immunological alterations, or hepatic disorders.[13] Indeed, this enzyme has been recently related with neurological disorders like Alzheimer's disease.[14,15] A large number of PTP1B inhibitor-based anti-diabetes molecules have been reported in the literature to date.[16–18] However, only non-competitive inhibitors have entered clinical trials *viz.* trodusquemine (NCT00509132), Ertiprotabib or JTT-551 (Figure 1).[19,20]
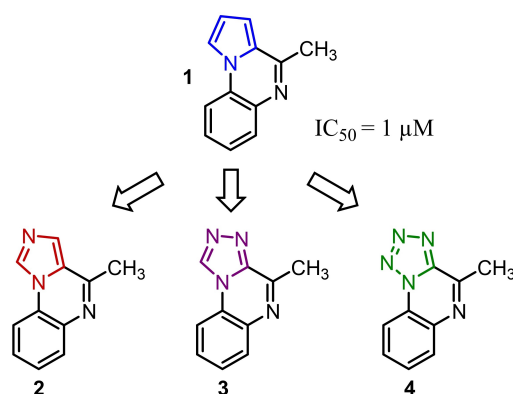
In this context, the research on PTP1B inhibition is an active field that aims to provide new insights into its function and therapeutic approaches with a plethora of inhibitors reported.[23–27] Scaffold-hopping strategies, which aim to identify iso-functional molecules with different main cores, form part of the current medicinal chemistry toolbox. This term, which was first used by Schneider in 1991,[28] has become a common medicinal chemistry and chemical biology technique that is widely employed in pharma and academia nowadays.[29] The objectives underlying these approaches are quite diverse, depending on the aims of the ongoing research and objectives. For example, scaffold-hopping is applied to improve activity, pharmacokinetic parameters or explore novel chemical and patentable space. However, its application depends on the target under investigation and the synthetic accessibility of the molecular designs. Nevertheless, although human intuition influences the scaffold-hopping process and the synthetic chemist takes part in the final decision, scaffold-hopping has essentially always been related to computational approaches like virtual screening, pharmacophore generation and similarity analysis.[30] As such, pharmacophores have been used to generate new PTP1B inhibitors by means of scaffold-hopping,[31,32] or even experience-driven scaffold-hopping, to yield compounds with IC_{50} values in the low micromolar range.[33] In a work reported by Saxena, authors identify through scaffold-hopping approaches interesting compounds from the point of view of their *in vivo* activities.[32] Nonetheless, despite the success of these works, in a great number of them, reported PTP1B inhibition activities in medium ranges. Besides, only one
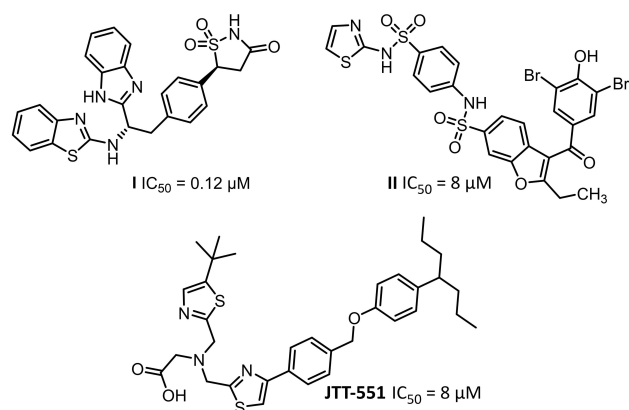
work by Shinde et al. performs virtual screening in the allosteric site of the enzyme with moderate results.[34] Another weakness of these approaches is that molecular docking, and pharmacophores do not provide a dynamic and so, a more realistic representation of the protein to account for effects such as induced fit and molecular recognition. In this regard, molecular dynamics (MD) simulations have become widespread in the field of drug design, and thank to the advances in GPU development and code improvements its incorporation into drug design work-flows has become very efficient, thus accelerating the drug-discovery process.[35]

Previous studies by our group have allowed us to identify hit **1** as a PTP1B inhibitor with good *in vitro* activity and putative binding to the allosteric cavity of this protein (see Supporting Information F1).[36] This site comprised a tunnel delimited by α-helixes 3, 6 and 7 in the C-terminal region of the soluble PTP1B enzyme.[21] However, **1** presents a high cLog*P* and highly aromatic carbon atoms, thus limiting its solubility and promoting undesired aggregate formation. As such, we propose the design of new candidates with, *a priori*, better properties by means of a scaffold-hopping strategy involving replacing the pyrrole ring with different azoles. Azoles with extra nitrogen atoms bearing an sp^2 lone pair are especially interesting given their ability, for instance, to form hydrogen bonds. Furthermore, incorporation of relatively electronegative nitrogen atoms in aromatic heterocycle may decrease its susceptibility to oxidative metabolism.[37] Thus, compounds **2**, **3** and **4**, which contain imidazole, 1,2,4-triazole and tetrazole rings, respectively (Figure 2), were considered as representative candidates for our starting hypothesis. To that end, we have designed a computational protocol that combines docking, MD and end-point free-energy calculations to estimate the behavior at a molecular level and generate possible PTP1B inhibitors.

Figure 1. Representative examples of PTP1B inhibitors and their IC_{50} values: pTyr mimetic (top left), allosteric inhibitors at the α3/α6/α7 site (top right) and a non-competitive inhibitor which entered Phase I clinical trials (bottom).[20–22]

Figure 2. Hypothesis for scaffold-hopping derivatization modification of 4-methylpyrrolo[1,2-*a*]quinoxaline.

ChemMedChem

Full Papers
doi.org/10.1002/cmdc.202100338

Chemistry Europe
European Chemical
Societies Publishing

Table 1. Predicted chemoinformatic properties of compounds **1–4**.

Compd	cLog$P$	TPSA [A^2]	ESOL Solubility [mg/mL][a]	Lipinski violations	Tanimoto similarity to **1**
1	2.79	17.30	0.036	0	1
2	2.19	30.19	0.103	0	0.60
3	1.58	43.08	0.24	0	0.54
4	0.98	55.97	0.84	0	0.46

[a] Predicted using SwissADME software (http://www.swissadme.ch/).

Results and Discussion

Computational design

Our scaffold-hopping approach was based on the replacement of the pyrrole ring by azoles. Transformation of the pyrrole ring into other azoles containing more nitrogen atoms leads to a significant variation in the physicochemical properties of the resulting azolo[1,2-*a*]quinoxaline scaffold. Thus, a decrease in cLog$P$ values is expected, as reflected in Table 1.

As a consequence, these proposed azoloquinoxalines would present a higher polarity, which would, in turn, increase their solubility in aqueous media given the increase in hydrogen bonding. This change is accompanied by a marked increase in TPSA (close to 60), while maintaining good values to promote cell permeability. Additionally, all proposed designs fulfil the Lipinski rules for oral absorption, thus making them interesting hit molecules with no functional groups and low molecular weights, thus allowing further complex derivatizations to generate lead compounds. To assess the impact of the azole moiety on the topology of the whole structure, a simple similarity analysis was carried out based on Morgan fingerprints. Interestingly, the similarity of the target compounds to **1** is dramatically decreased, especially for **4**. As shown in Table 1, the greater the number of sp^2 nitrogen atoms with a sp^2 lone pair, the lower the Tanimoto similarity index, thus a significant change in biological activity might be expected comparing with hit **1**. Even in the case of a considerably lower similarity to the starting compound **1**, the substitution of an sp^2 carbon by nitrogen atoms may act as a strategy to block metabolically labile positions in the five-membered ring, thus maintaining the desired activity. A similar bioisosteric replacement, has proved to be more useful, even for multiparameter optimization, especially in ADMET properties.[38]

All in all, these data suggest that these new compounds present better drug-like properties, especially as regards their increased solubility without impairing permeability. The predicted pharmacokinetic profile and drug-like properties for these hits were also evaluated by means of *in silico* tools to support this hypothesis (see Supporting Information). All the proposed structures showed low molecular weight (<500) and suitable surface area values (Table 1). There were not any PAINS alert for these molecules and regarding drug-like properties, there were no violation in terms of 'Rule of Five' by Lipinski and related. Finally, the predicted gastrointestinal absorption was predicted to be high (see Supporting Information S2–S5).

Considering aforementioned data, which support the interest of these candidates, we modelled the target azoles **2–4** as well as **1** on PTP1B by means of docking and conventional molecular dynamics approaches to gain a deeper insight into the molecular-recognition process at an atomic level.

In previous studies on the pyrrolo[1,2-*a*]quinoxaline system, experimental and extensive computational modelling let us propose that these molecules would bind to the allosteric cavity of PTP1B.[36] In consequence, for the present work, we modelled these compounds into the same pocket. The shape and aromatic properties of these scaffolds fit quite well into the allosteric cavity of PTP1B, and as such, they tend to establish the same interactions as the benzbromarone core of PTP1B inhibitors described by Wiesmann et al. (see Supporting Information F1).[21]

Docking experiments revealed two different binding modes. As illustrated for **1**, the imidazoquinoxaline **2** and the triazoloquinoxaline **3** shared the same binding mode (Figure 3). This is stabilized by several π-π stacking interactions mediated
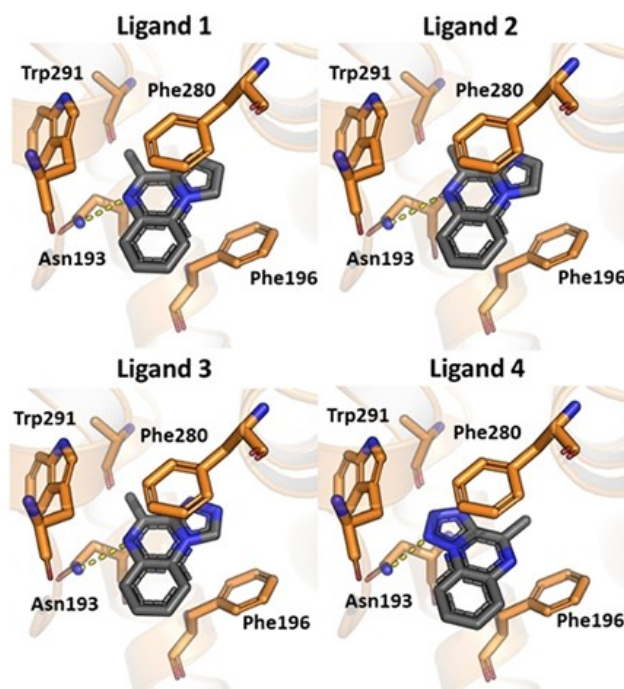
Figure 3. Docking poses obtained for compounds **1–4** in the homology model generated for PTP1B. The hydrogen bonds found between the ligands and Asn193 in PTP1B are depicted as dashed yellow lines.

ChemMedChem

Full Papers
doi.org/10.1002/cmdc.202100338

Chemistry
Europe
European Chemical
Societies Publishing

by the scaffold with Phe196 (α3 helix) and Phe280 (α6 helix). In addition, a parallel-displaced interaction with Trp291 (α7 helix) could be observed, as well as a CH-π interaction between the hydrogens of the methyl group and the pyrrole ring of Trp291. Finally, as a directional leading force, the nitrogen lone pair of the quinoxaline moiety is hydrogen bonded to the Asn193 side chain (α3 helix). In contrast, a different scenario was observed for the tetrazolo derivative **4**. In this case, π-π interactions are established with the aromatic residues of the allosteric site, and a hydrogen bond is formed with one of the nitrogen atoms of the tetrazole ring (Figure 2). This different binding mode can be partially explained by a better geometry of the interaction (2 Å long and a θ angle of 177°, see Supporting Information). On the other hand, a second binding mode, which orients the methyl group towards a small gap in a similar fashion as the ethyl substituent in benzbromarone derivatives (PDB: 1T48, 1T4J, 1T49), in order to gain van der Waals interactions was observed for **4**.

Overall, it seems that the proposed analogues are able to maintain the same key binding patterns as cognate ligands previously described in the literature.

Although molecular docking may provide a useful description for the interaction between a protein and a ligand at a molecular level to establish a first approach, other computational techniques may also provide valuable and extensive information.

Thus, molecular dynamics (MD) simulations allow the study of a target protein over a pre-defined time. Consequently, MD can be used as a refinement protocol for docking poses to study which binding mode is more plausible and the likelihood that it is stable in physiological media. Moreover, MD studies have been extensively incorporated into drug-design workflows and free-energy calculations for hit-to-lead optimizations.[39,40]

In this context, we decided to perform MD simulations to gain an in-depth insight into the molecular-recognition phenomena between our molecular designs and PTP1B in order to evaluate potential effects on the target and to support our hypothesis.

Since the crystal structure of PTP1B bound to an allosteric ligand has not been completely solved, homology model techniques were employed to generate a complete α7 helix PTP1B for our purposes. This fact is in part due to the destabilizing effect of ligands on the α7 helix that triggers and propagates the allosteric signaling over the protein, which leads to a blocking of the WPD loop in its open form.

Initially, in order to lay the groundwork for our subsequent simulations, a control simulation of the PTP1B in its apo form (without any ligand) was carried out starting from the open WPD loop conformation to study the system behavior in solution. Monitoring of the root-mean-square deviation (RMSD) values allowed us to conclude that the protein readily reached an equilibrium state after approximately 50 ns, with a mean value of around 1.8 Å (Figure 4). Furthermore, a root-mean-square fluctuation (RMSF) plot for Cα did not show significantly high values, except for those residues located in the α7 helix, as previously observed in the literature [3, 41].
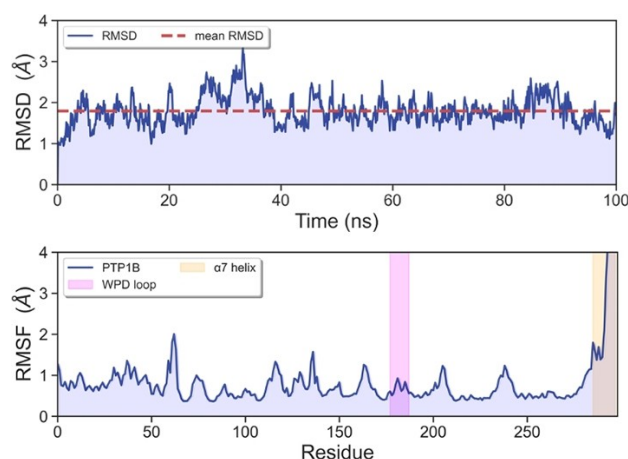

Figure 4. Cα backbone RMSD (top) and Cα RMSF (bottom) plots for the PTP1B MD simulation at 100 ns.

After checking that our protocol worked with apo PTP1B, we performed four more simulations for complexes PTP1B-**1** to PTP1B-**4**, starting from the molecular docking coordinates. These simulations showed that PTP1B remained stable, with RMSD plots similar to those for the apo form (see Supporting Information, F6) that remained relatively unchanged along the trajectory. The overall Cα RMSDs for the protein structures relative to the respective starting coordinates during these simulations are 2.35, 2.7, 2.02 and 1.5 Å for complexes PTP1B-**1** to PTP1B-**4**, respectively. According to these values, a more mobile structure arises upon complexation of PTP1B to ligands **1**, **2** and **3** compared with **4**, as deduced from the higher RMSD mean values. These data suggest that complexation of PTP1B with **4** does not produce an extensive structural rearrangement in the whole protein. As a consequence, compound **4** might exert a lower impact on allosteric mechanism propagation along the PTP1B backbone and in the final inhibition compared with **1**–**3**.

Similarly, the RMSFs also tended to be very similar to that for apo the form, thus corroborating the stability of the system (see Supporting Information, F7). The mobile parts of the enzyme corresponded mainly to loops, while the rest of the secondary structural elements remained more rigid. As far as the WPD loop is concerned, the RMSF values for the simulations were similar. As a consequence, we concluded that our models are able to capture a stabile form of the catalytic loop in its open inactive conformation, as described previously.[41,42]

A different picture was found when ligands **1**–**4** were studied in detail. In general, the designed molecules remained inside the allosteric cavity during the 100 ns, thus supporting the hypothesis of the binding site, and all of them maintained the hydrogen bond with Asn193 during most of the simulations. Our results show that the proposed binding modes, which are stable over 100 ns of conventional MD simulation, are dominated by van der Waals and hydrophobic interactions. Despite this, small fluctuations, which eventually led to shifts of the ligands in the pocket, as reflected in the RMSD values, were

ChemMedChem

Full Papers
doi.org/10.1002/cmdc.202100338

**Chemistry
Europe**

European Chemical
Societies Publishing

detected (Figure 4), but no unbinding event was observed. The π-π interactions are also well maintained during the simulations, especially for Phe192 and Phe280. Indeed, this latter has been claimed to be a key anchoring residue for PTP1B allosteric inhibitor binding and stabilization.[21,41,43] However, the interactions involving Trp291 (α7 helix) change during the dynamics, mainly due to the high mobility of this part of the protein. An unexpected finding emanating from the present simulations was obtained in the case of **4**. In this case, after just 4 ns from the beginning, this compound suffered a change in its binding mode. This event led to a new reorientation of **4** in the binding site to the same binding mode observed for ligands **1**–**3** (Figures 5A and 5B). Thus, the nitrogen of the quinoxaline core establishes a hydrogen bond with the Asn193 side chain until the end of the simulation. These findings support the hypothesis about the binding mode of these compounds, which was dilucidated by docking for ligands **1**–**3**. Moreover, the Ala189 and Ile281 side chains contribute to binding via van der Waals interactions during the MD simulation.

These simulations were useful for evaluating the potential of our designs to remain bound to the PTP1B and to refine the poses obtained during docking experiments. However, a detailed analysis of the geometry of the allosteric tunnel may support the allosteric mechanism of inhibition.

The allosteric cavity is delimited by the three alpha helixes α3, α6 and α7 (Figure 6A). The presence of a ligand leads to a partial displacement and destabilization of the α7 helix in order to accommodate the ligand. This fact has been extensively studied previously using computational approaches and is supported by the lack of fully solved PTP1B-inhibitor crystal structures. In fact, α7 helix movement and destabilization has previously been considered to be a marker for the allosteric signaling effect in PTP1B.[36,44,45] As such, we measured the mean RMSD values for the α7 helix to compare its stability among
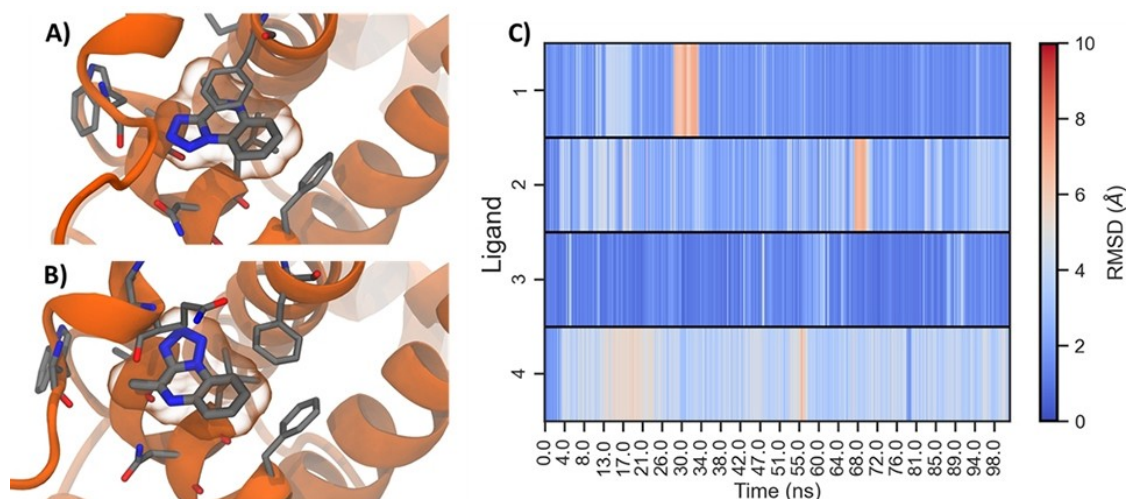
Figure 5. Snapshot of ligand **4** taken from 2 ns (A) and 10 ns (B) of conventional MD simulations. RMSD heatmap plot of ligands **1**–**4** across 100 ns of simulation time.
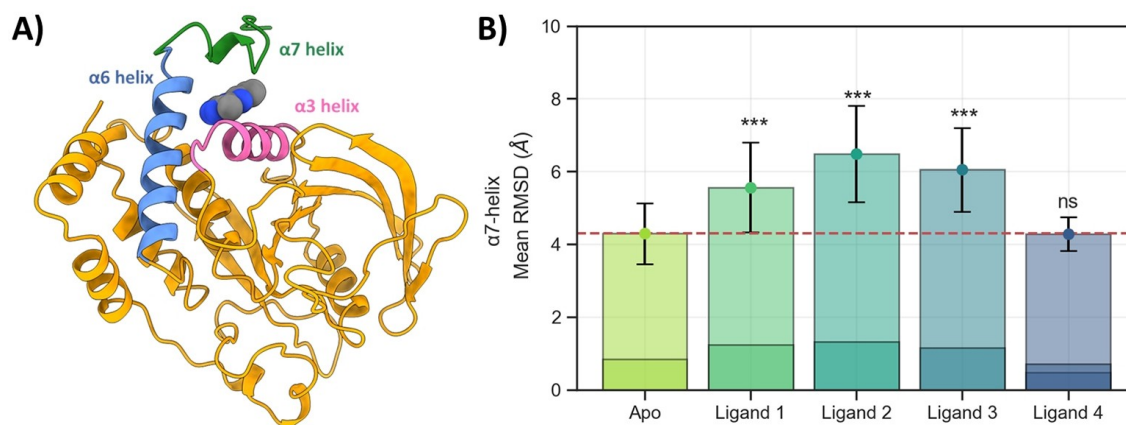
Figure 6. A) PTP1B cartoon representation of PTP1B bound to ligand **3**. B) Mean RMSD bar plot calculated for the α7 helix across the simulation. Results are the mean ± SD. ***$p \leq 0.001$, ns = not statistically significant. Statistical significance was carried out by performing t-test between Apo RMSD and each of the PTP1B-ligand simulations.

ChemMedChem

Full Papers
doi.org/10.1002/cmdc.202100338

Chemistry Europe
European Chemical
Societies Publishing

Table 2. Per-term MM-ISMSA energy decomposition calculated for ligands **1–4** over the last 50 ns of MD simulation (kcal/mol).

Compd	Total energy	Van der Waals	Coulombic	Compd desolvation	PTP1B desolvation	Apolar
1	-30.69 ± 2.34	-29.42 ± 0.51	-2.00 ± 0.28	1.83 ± 0.12	1.05 ± 0.33	-2.14 ± 0.073
2	-32.73 ± 3.35	-31.72 ± 0.62	-1.51 ± 0.22	1.71 ± 0.13	0.95 ± 0.7	-2.17 ± 0.09
3	-30.70 ± 2.81	-29.29 ± 0.48	-1.37 ± 0.24	2.21 ± 0.21	-0.13 ± 0.58	-2.10 ± 0.11
4	-30.69 ± 3.27	-30.92 ± 0.66	-0.77 ± 0.07	1.42 ± 0.17	1.78 ± 0.78	-2.20 ± 0.084

simulations (Figure 6B). Thus, while apo PTP1B presented a mean value of 4.29 Å, **1**, **2**, and **3** gave considerably higher RMSDs, as shown in Figure 6. However, this effect was not observed for **4** (mean RMSD = 4.28 Å) in our simulation. Although the analysis of these findings should not be considered statistically significant, during simulation, ligand **4** exhibited the highest fluctuation inside the cavity (Figure 5), therefore its weaker binding might exert a lower destabilizing effect on the PTP1B α7 helix.

In summary, all the MD results also suggest a good scenario for the candidates and their putative binding to PTP1B.

Finally, we also calculated the binding free energy of our candidates to PTP1B to assess their potential as a tight, medium or weak binder. To this end, we selected the ultra-fast method MM-ISMSA, which has been developed to estimate the free binding energy between protein-protein or protein-ligand partners in a similar fashion as other, more computationally demanding methods such as MMGSA and MMPBSA or the perturbation and thermodynamics integration procedures. The predicted binding energies for all complexes are dominated by van der Waals and hydrophobic interactions, as depicted in Table 2. This is in good agreement with previous studies that reported estimated values for the binding free energy between allosteric ligands and PTP1B.[43] Remarkably, the values obtained for all four complexes are quite similar. This fact highlights the potential of our designs **2–4** to bind PTP1B with good affinity, thus suggesting inhibitory activity. According to this, all ligands should present similar affinities to **1**, except imidazoquinoxaline **2**, which should exert a better value.

Inspection of the per-residue energy decompositions highlighted the importance of the ligand environment for binding (Figure 7). Thus, residue Asn193 makes a marked contribution to the binding free energy in all complexes, as expected for a hydrogen-bond interaction, followed by aromatic residues such as Phe196, Trp291 and hydrophobic residues Leu192 and Ala189. Interestingly, this method was able to highlight the importance of the Phe280 residue, which has also been described previously, thereby supporting and validating these simulations.[41,43]

Chemistry

Based on the aforementioned computational workflow and its conclusions, we established that application of the scaffold-hopping strategy to the pyrrole ring may provide interesting candidates for PTP1B inhibition. As such, we prepared the three
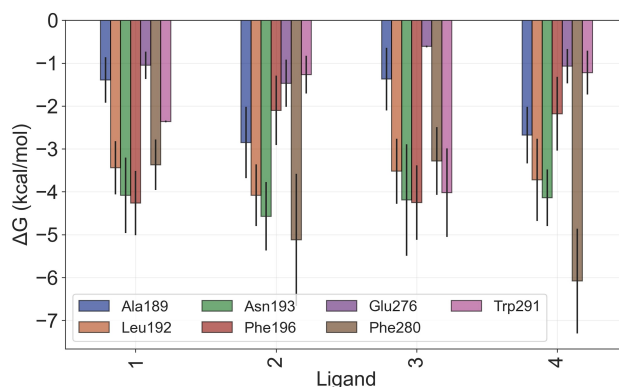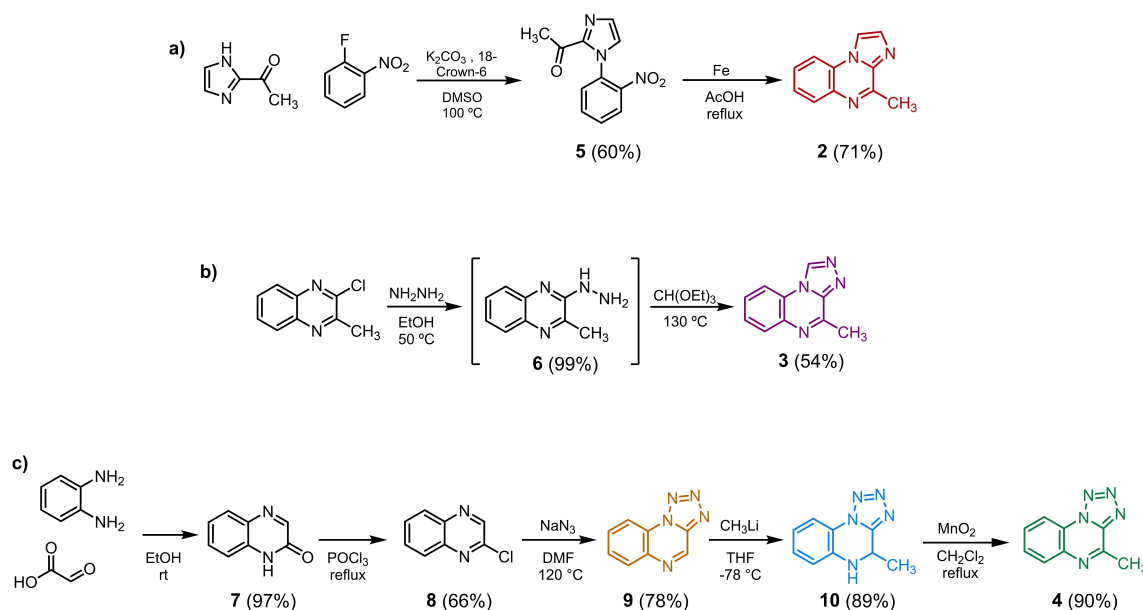

Figure 7. Calculated energy contributions of individual complexes residues to the overall binding free energy.

proposed candidates **2–4** by setting up a multistep synthetic procedure based on previously described protocols.

The synthesis of 4-methylimidazo[1,2-*a*]quinoxaline (**2**) was carried out by nucleophilic substitution of 2-nitrofluorobenzene with 2-acetylimidazole in basic media to give **5**, and following reduction of the nitro group by iron and *in situ* cyclisation, obtaining the final product with good yield (Scheme 1a).

To prepare **3** and **4**, we adapted protocols previously described in the literature, using commercially available 2-chloro-3-methylquinoxaline as the starting material for triazole ring construction and cyclisation,[46,47] thus **6** was first obtained by treatment with hydrazine and subsequent cyclisation in the presence of trimethyl orthoformate at 130 °C via the iminium cation (Scheme 1b). Further experiments showed that hydrazine intermediate **6** need not be isolated, thus avoiding one chromatography step and obtaining the desired final product in reasonable yield.

For the synthesis of tetrazole **4**, we explored a different synthetic pathway. In this case, we prepared 2-chloroquinoxaline **8** by condensation of commercially available *o*-phenylendiamine with pyruvic aldehyde at room temperature. After treatment of **7** with phosphorous oxychloride, **8** was easily obtained. This intermediate was subsequently converted into tetrazoloquinoxaline **9** by treatment with NaN_3 in DMF. The product thus obtained was then methylated with methyllithium at low temperature to afford 4-methyl-4,5-dihydrotetrazolo[1,5-*a*]quinoxaline (**10**). Finally, **4** was easily obtained in excellent yield by oxidation of **10** with activated MnO_2 (Scheme 1c).

ChemMedChem

Full Papers
doi.org/10.1002/cmdc.202100338

**Chemistry
Europe**
European Chemical
Societies Publishing

Scheme 1. a) Synthesis of 4–methylimidazo[1,2-*a*]quinoxaline; b) synthesis of 4-methyl[1,2,4]triazolo[4,3-*a*]quinoxaline; c) synthetic route to generate tetrazolo [1,5-*a*]quinoxaline derivatives.

Biological evaluation

Once we prepared the desired compounds, we assessed their PTP1B inhibitory effects *in vitro* using the commercially available soluble 322 amino acids enzyme. Since our synthetic approach led to the isolation of two extra azolo derivatives (**9** and **10**), we included them in these experiments (Table 3). Compound **1** had already been evaluated against PTP1B with an IC$_{50}$ of 1.00 μM.[36] The remaining compounds showed a good inhibitory activity within a relatively narrow low- and sub-

Table 3. *In vitro* data obtained for compounds **1–4**, **9** and **10**.

Compd	Structure	IC$_{50}$ ± SD [μM]	pIC$_{50}$	% Inhib. PTP1B @ 1 μM[b]	% Inhib. TCPTP @ 1 μM[b]	SI[c]
1		1[a]	6	51	54	0.94
2		0.46 ± 0.04	6.33	87	44	1.97
3		0.79 ± 0.01	6.1	70	55	1.27
4		1.48 ± 0.07	5.82	46	50	0.92
9		0.62 ± 0.2	6.2	80	68	1.17
10		2.17 ± 0.08	5.66	37	35	1

[a] From Reference [34]. [b] Percentage of enzyme inhibition at 1 μM. [c] SI = selectivity index, is defined here as percentage inhibition ratio PTP1B/TCPTP at 1 μM.

micromolar IC$_{50}$ range. Of all the compounds proposed, **2** showed the highest potency (pIC$_{50}$=6.33), in all the series (minimum pIC$_{50}$ of 5.66 for compound 10). This is in good agreement with the free energy predicted using the MM-ISMSA method, which indicated that this compound stands out from the others in terms of total binding free energy (Table 2). In addition, **3** also showed a marked ability to inhibit the enzyme. In contrast, the worst inhibitory effect was obtained for tetrazolo derivative **4** (IC$_{50}$=1.48 μM). However, these findings are also valuable from the point of view of our computational model, which predicted a worse behavior during MD experiments. It should be noted that compound **9** showed a very good IC$_{50}$, whereas the dihydro derivative of **4** (compound **10**) showed the worst value for all the compounds synthesized herein. As a consequence, compound **10** is the least interesting from the point of view of optimization and hit-to-lead because of its low potency (pIC$_{50}$=5.66).

We also carried out an initial selectivity evaluation of these compounds against T cell protein-tyrosine phosphatase (TCPTP), the closest homologue to PTP1B with a 72% of shared sequence identity.[48] Inhibition of this enzyme should be take into account as a check point during PTP1B development, as it is responsible of very dangerous effects observed in murine models such as blood abnormalities, inflammation and subsequent death.[49]

In our *in vitro* experiments, all molecules inhibited this enzyme, as shown in Table 3. However, for compounds **2**, **3** and **9**, higher inhibition for PTP1B rather than TCPTP was observed at the same concentration (SI >1). Only **2** displayed approximately two times selectivity for PTP1B over TCPTP, whilst **4** and **10** turned out to be non-selective (SI≤1). This behavior is, in part, expected since these derivatives lack of functional groups and present a relatively simple structure, similar to hit **1** which was non-selective (SI=0.94). Given these results, future optimization of these hits should also consider addressing the selectivity issue over TCPTP to avoid undesired side effects in this related off-target.

Finally, to provide an added value to our breakthroughs we decided to explore the phenotypic efficacy of some relevant compounds in *ex vivo* assays. Although IC$_{50}$ is a good marker for evaluating the potency of compounds against an enzymatic target, cellular assays can be used to establish the utility and efficacy as regards the mechanism of action and desired effects. With this in mind, we investigated whether our compounds are able to modify glucose uptake in cellular models. Our most promising candidates in terms of pIC$_{50}$ (derivatives **2** and **3**) were selected for this more sophisticated experiment.

The insulin mimetic activity was evaluated by using insulin as positive control. This latter was included in the assays to compare to basal conditions the ability of cells to increase glucose uptake. This experiment showed that both compounds induced a slight but statistically significantly increased glucose uptake by cultured myotubes that are cells particularly sensible to insulin actions on glucose metabolism (Figure 8). Interestingly, the effects on glucose uptake from both compounds did not reflect their ability to inhibit PTP1B activity. Whilst compound **2**, with the best pIC$_{50}$, only increased glucose by
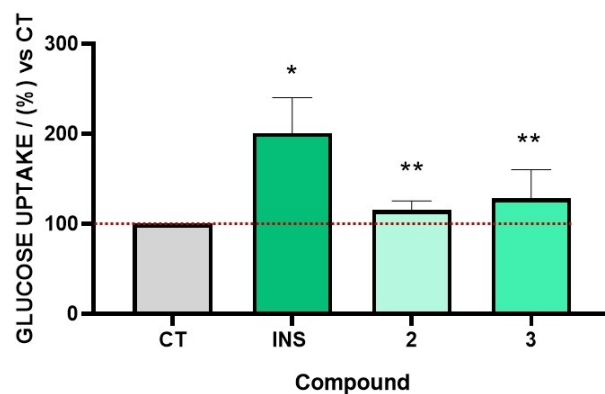
Figure 8. Effect of inhibitors **2** and **3** on glucose uptake in C2 C12-based myotubes. Cells were incubated with vehicle (CT), insulin (INS, 10 nM, 30 min) compounds **2** or **3** (2 μM, 90 min), and the fluorescent oxyglucose analog 2-NBDG (0.1 mM) was added for an additional 30 min period. Changes in intracellular fluorescence reflect glucose uptake, and they were referred to glucose uptake by their respective controls (CT). Date are the mean ± S.E.M of 5 independent experiments. *$p < 0.05$ vs CT. **$p < 0.05$ vs CT and INS.

15% with respect to control cells, compound **3** exhibited about a 30% of increment. Given these data, both compounds, may be of therapeutical interest for further development, based in its phenotypic effects which confirm they ability to produce an *ex vivo* response aimed to decrease glucose content outside the cell.

Conclusion

PTP1B is considered to be a promising target for the treatment of type 2 diabetes mellitus, metabolic syndrome and other conditions. Studies carried out into this target and its biochemical roles are still of interest for the scientific community, as is the synthesis of new chemical probes and drugs for its inhibition and subsequent study. Despite not being particularly novel approaches, scaffold-hopping strategies are of particular interest for this purpose due to their ability to provide new chemotypes with tailored physicochemical properties for different objectives. In this work, we have designed a computational workflow that includes a simple chemoinformatic analysis of the pyrrolo[1,2-*a*]quinoxaline scaffold and further validation by means of docking and MD approaches. Molecular docking suggested a similar pattern of molecular recognition compared to previously described and characterized cognate inhibitors. Additionally, MD simulation allowed us to study the molecular determinants of the interactions and predict the suitability of our designs. We have also used the MM-ISMSA algorithm to predict binding free energy, obtaining similar results to others described previously and documented in the literature, thereby validating its utility for the study of PTP1B. This whole implementation has allowed us to find new derivatives bearing imidazole, 1,2-4-triazole and tetrazole rings fused to the side (*a*) in the quinoxaline core, which maintain and even improve its PTP1B inhibitory activity and are in very good agreement with

ChemMedChem

Full Papers
doi.org/10.1002/cmdc.202100338

Chemistry Europe
European Chemical
Societies Publishing

our simulations. Additionally, to the best of our knowledge, this is the first time that MM-ISMSA has been applied to a scaffold-hopping strategy to obtain good concordance with *in vitro* results. Furthermore, the cheap computational requirements of this algorithm to calculate binding free energy, it become in a very attractive tool for drug discovery purposes. Moreover compounds **2** and **3** are very interesting for hit optimization because they are selective for PTP1B rather than TCPTP. Finally, these two derivatives have been shown to increase glucose uptake in phenotypic models, thus validating this approach and, confirming the relevance of these fragments for further optimization and development. As such, scaffoldhopping strategies aimed to exchange the pyrrole ring in the nucleus of pyrrolo[1,2-*a*]quinoxaline core by the studied azoles may be of interest to obtain novel chemotypes with similar activities and different physicochemical properties. These results also bring an opportunity to select the most suitable scaffold, according to the synthetic accessibility purposes, while preserving its inhibitory properties towards PTP1B.

Experimental Section

Computational methods

Ligand preparation and analysis. All ligands were generated using the corresponding smiles codes generated with MarvinSketch 21.3, ChemAxon (https://www.chemaxon.com). Thereafter, RDKit, was used to add hydrogens and generate minimized 3D coordinates for all compounds using our in-house scripts. For similarity analysis with RDKit (http://www.rdkit.org), Morgan fingerprints of radius 2 and 1240 bytes (MFP2) were selected, then the Tanimoto similarity was calculated. Statistical analysis was carried out using the Python SciPy library.[50] ADME and physicochemical properties were calculated using web server SWISS-ADME (http://www.swissadme.ch/).

Ligand docking. Docking was performed using the GOLD engine program as implemented in Hermes. For docking purposes, a homology model of PTP1B with a whole α7 helix in the allosteric site was generated, as described previously.[36,41] Briefly, a homology model was constructed with the sequence of whole PTP1B (UniProt ID: P18031) using as template PDB: 1T48 in SWISS-MODEL (https://swissmodel.expasy.org/), then protonation states were investigated with H++ webserver (http://biophysics.cs.vt.edu/hppdetails.php). The binding site was defined as being 6 Å away from the coordinates of the ligand BB3 (PDB: 1T48). The genetic algorithm search option was set to slow (more accurate) and early termination was allowed if the number of GA runs in the top 5 solutions were within 1 Å. The remaining parameters were set as default.

Molecular dynamics. Protein topology was described using Amber ff14SB,[51] while the GAFF forcefield was chosen for ligands.[52] To parameterize small molecules, an AM1-BCC model of RESP charges[53] was generated using sqm in antechamber.[54] The, tleap module implemented in Ambertools16,[55] was used to solvate the systems with a TIP3P cubic water box extending 10 Å away from the solute. After this, five sodium ions were added to the system in order to achieve a neutral charge. The topology and coordinates files were submitted to a multi-step minimization, thermalization and equilibration using the Sander engine, following previously described protocols.[41] All-atom classical molecular dynamics simulation were then carried out with the OpenMM software.[56] All simulations used a Langevin integrator with a temperature of 310 K

and a friction coefficient of 1 ps-1. Long-range electrostatic interactions were treated with the particle mesh Ewald method, with constraints for all bonds involving hydrogen. Production dynamics was carried out in the NPT ensemble using a Montecarlo Barostat (1 atm) and a 2-fs time step. The OpenCl platform in single precision mode was selected as engine for MD. Simulations were performed on a Windows Workstation with a Nvidia® Gigabyte GeForce RTX 2060 GPU, yielding a max performance of 122 ns/day.

Binding energy calculations were performed using the ultrafast software MM–ISMSA compiled for Windows 64-bit systems.[57] To this end, 500 snapshots were taken from the last 50 ns of MD trajectories for each system, corresponding to equilibrated structures. This software allows the solvent-corrected binding energies to be estimated for the same sets of coordinates, as well as their per-residue free energy decompositions into van der Waals, coulombic, apolar, and desolvation terms.

MD analysis was performed using MDtraj,[58] MDAnalysis[59] and Pandas python libraries.[60] Protein Cα atoms were aligned to the starting conformation of the simulation to calculate RMSD and RMSF values. Graphics were generated with Matplotlib[61] and Seaborn.[62] Simulation and image rendering were carried out with VMD,[63] Chimera X[64] and PyMOL (The PyMOL Molecular Graphics System, Version 2.1 Schrödinger, LLC).

Chemistry

All reagents were acquired from the following commercial sources and used without further purifications: Merck, ACROS, Novabiochem and Fluorochem. Solvents were purchased from Scharlab and EtOAc, Hexane and CH_2Cl_2 were distilled prior to use. Dry solvents were obtained using an MBRAUN MB-SPS-800 device. For those reactions which were performed under inert atmosphere, argon or nitrogen were used with oven-dried glassware, magnetic stirring and dry solvents.

Reactions were followed by thin layer chromatography (TLC) on Merck Kieselgel 60 F254 0.25 mm precoated aluminum plates. TLC plates were visualized using UV light ($\lambda = 254$ nm or 365 nm) and/or staining with Ninhydrin (1 M, EtOH), 1% aq. $KMnO_4$ or phosphomolybdic acid (0.05 M, EtOH). Purification was carried out by normal-phase silica gel flash chromatography, using gel grade 60 (70-230 mesh, Merck). High-resolution analyses (HRMS) were performed on an Agilent 6210 time of flight LC/MS using electrospray (ESI) as ion source and a mobile phase of ACN/H_2O 75:25 with 0.1% TFA as additive. The HPLC column (50 mm×4.6 mm) contained a C18 stationary phase with a particle size of 3.5 μm. Compounds were >95% pure High-resolution mass spectra were recorded on an Agilent 6210 LC/MS TOF mass spectrometer. Data are expressed as mass units (z/e). ^{1}H and ^{13}C NMR spectra were recorded on a either a Varian Mercury VX-300, Varian Unity 300 or Varian Unity 500 MHz spectrometer at room spectrometer in the deuterated solvent stated. Chemical shifts (δ) are quoted in parts per million (ppm) and using the residual non-deuterated solvent signal as an internal reference. Multiplicities are denoted as singlet (s), doublet (d), triplet (t), quartet (q) and multiplets as (m). Coupling constants (*J*) are given in Hertz (Hz).

2-Acetyl-1H-1-(2-nitrophenyl)imidazole (**5**). 2-Acetyl-1*H*-imidazole (100 mg, 0.9 mmol, 1 equiv), anhydrous K_2CO_3 (139 mg, 0.99 mmol, 1.1 equiv), and 18-crown-6 (523 mg, 1.98 mmol, 2.2 equiv) were added to an oven-dried Schlenk flask provided with a stir bar. The air was then evacuated under vacuum and the Schlenk flask purged with argon. Anhydrous DMSO (5 mL) was added, followed by 1-fluoro-2-nitrobenzene (139 mg, 0.99 mmol, 1 equiv). The resulting mixture was heated to 100 °C and stirred for 3 h. The reaction mixture was then cooled to room temperature, diluted with H_2O

ChemMedChem

Full Papers
doi.org/10.1002/cmdc.202100338

Chemistry Europe
European Chemical
Societies Publishing

(27 mL) and extracted with CH_2Cl_2 (3×10 mL). The organic layer was dried over anhydrous Na_2SO_4, the solvent was removed under vacuum, and the product was purified by flash column chromatography on silica gel (CH_2Cl_2/acetone 9:1) to give **5** as a yellowish solid. Yield: 126 mg, 0.54 mmol, 60%; ^{1}H-NMR (500 MHz, CDCl$_3$): δ 8.19 (dd, $J=8.0$, 1.7 Hz, 1H, Ar-H6), 7.73 (td, $J=7.6$, 1.7 Hz, 1H, Ar-5), 7.65 (td, $J=7.6$ Hz, 1H, Ar-H4), 7.38 (dd, $J=8.0$, 1.6 Hz, 1H, Ar-H3), 7.35 (s, $J=1.2$ Hz, 1H, HetAr-H5), 7.15 (d, $J=1.1$ Hz, 1H, HetAr-H5), 2.63 (s, 3H, CH$_3$); ^{13}C-NMR (125 MHz, CDCl$_3$): δ 204.17 (CO), 149.54 (Ar-C2), 138.30 (Ar-C2), 134.44 (ArC), 133.02 (ArC), 133.00 (ArC), 130.89 (Ar-C1), 130.47 (ArC), 129.55 (Ar-C1′), 126.49 (C-Ar5′′), 126.04 (Ar-C4′′), 27.31 (CH$_3$); HRMS (ESI-TOF) m/z calculated for $C_{11}H_{10}N_3O_3$ $[M+H]^+$: 232.0717. Found $[M+H]^+$: 232.0718.

4-Methylimidazo[1,2-a]quinoxaline (**2**). Fe powder (52 mg, 0.92 mmol, 4 equiv) was added to a solution of **5** (55 mg, 0.23 mmol, 1 equiv) in AcOH (3 mL). The system was then purged with argon and the reaction mixture refluxed for 3 h until end of the reaction (TLC monitoring). The reaction mixture was subsequently cooled to room temperature and the solution neutralized with satd. NaHCO$_3$ (5 mL). The aqueous phase was extracted with CH_2Cl_2 (3×10 mL) and the organic extracts were pooled and dried (MgSO$_4$). The desiccant was filtered off and the solvent was removed under reduced pressure to give a residue that was chromatographed on silica gel (CH_2Cl_2/methanol 9.5:0.5) as eluent to afford **2** as a cream colored solid. Yield: 30 mg, 71%; M.P.: 81–83 °C; ^{1}H-NMR (500 MHz, CDCl$_3$): δ 8.09 (d, $J=1.1$ Hz, 1H, H1), 8.03 (td, $J=5.4$, 1.3 Hz, 1H, H2), 7.85 (dd, $J=7.7$, 1.8 Hz, 1H, H6), 7.76 (d, $J=1.1$ Hz, 1H, H9), 7.64–7.53 (m, 2H, H7 and H8), 2.98 (s, 3H, CH$_3$); ^{13}C-NMR (125 MHz, CDCl$_3$): δ 146.37 (C4), 139.4 (C3a), 135.7 (C5a), 129.61 (C6), 128.63 (C8), 127.03 (C9a), 126.81 (C7), 114.69 (C9), 112.73 (C1), 29.74 (CH$_3$). HRMS (ESI-TOF) m/z calculated for $C_{11}H_{10}N_3$ $[M+H]^+$: 184.0869. Found $[M+H]^+$: 184.0867.

4-Methyl[1,2,4]triazolo[4,3-a]quinoxaline (**3**). Compound **6** (110 mg, 0.559 mmol) was dissolved in triethyl orthoformate (4 mL) and the reaction mixture stirred at 130 °C overnight before being cooled to room temperature. The reaction mixture was concentrated under reduced pressure and the residue thus obtained was purified by column chromatography on silica gel (CH_2Cl_2/MeOH, 9:1) to give 3 as an orange solid. Yield: 55 mg, 54%; M.P.: 129–131 °C; ^{1}H-NMR (500 MHz, CDCl$_3$): δ 9.28 (s, 1H, H1), 8.09 (dd, $J=7.1$, 2.4 Hz, 1H, Ar-H6), 7.97–7.85 (dd, $J=7.2$, 2.2 Hz, 1H, H9), 7.75–7.60 (m, 2H, H7 and H8), 3.06 (s, 3H, CH$_3$); ^{13}C-NMR (125 MHz, CDCl$_3$): δ 148.31 (C4), 145.86 (C3a), 139.26 (C1), 131.58 (C5a), 130.32 (C7), 130.25 (C8), 129.17 (C6), 128.17 (C9a), 115.29 (C9), 21.42 (CH$_3$). Spectroscopic data and melting point agree with those reported in the literature.[46]

4-Methyltetrazolo[1,5-a]quinoxaline (**4**). Activated MnO$_2$ (116 mg, 1.535 mmol) was added to a solution of **10** (50 mg, 0.267 mmol) in CH_2Cl_2 (11 mL/mmol) and the suspension stirred for 2.5 h. After this time, the reaction mixture was filtered through a pad of Celite® and the solvent eliminated under reduced pressure to afford **4** as an amorphous yellowish solid. Yield: 44 mg, 90%; M.P.: 146–148 °C; ^{1}H-NMR (500 MHz, CDCl$_3$): δ 8.55 (dd, $J=6.3$, 3.2 Hz, 1H, H6), 8.18 (dd, $J=6.1$, 3.3 Hz, 1H, H9), 7.92–7.68 (m, 2H, H7 and H8), 3.12 (s, 3H, CH$_3$); ^{13}C-NMR (125 MHz, CDCl$_3$): δ 151.27 (C4), 145.87(C3a), 136.37 (C5a), 132.25 (C6), 130.52 (C9a), 130.00 (C8), 129.88 (C7), 116.48 (C9), 22.26 (CH$_3$). Spectroscopic data and melting point agree with those reported in the literature.[46]

Tetrazolo[1,5-a]quinoxaline (**9**). Sodium azide (2 equiv) was added to a suspension of **8** (300 mg, 1.62 mmol) in DMF (1.85 ml/mmol). The flask was then purged with argon and heated to 120 °C for 24 hours. After cooling to room temperature, the mixture was poured into an ice/water (61 mL/mmol) bath and the aqueous layer extracted with EtOAc (3×10 ml) and washed with water (3×10 mL),

followed by brine (10 mL). The organic layer was dried over anhydrous Na_2SO_4, and the solvent was evaporated under reduced pressure. The residue was purified by flash chromatography over silica gel (EtOAc/hexane, 1:1) to afford **9** as an orange solid. Yield: 50 mg, 78%; M.P.: 126–128 °C; ^{1}H-NMR (300 MHz, CDCl$_3$): δ 9.58 (s, 1H, H4), 8.67 (d, $J=7.8$ Hz, 1H, Ar-H6), 8.34 (d, $J=7.9$ Hz, 1H, H9), 8.01–7.78 (m, 2H, H7 and H8). Spectroscopic data and melting point agree with those reported in the literature.[47]

4-Methyl-4,5-dihydrotetrazolo[1,5-a]quinoxaline (**10**). Methyllithium (1.6 M in hexane, 9.6 mg, 0.438 mmol) was added to a solution of **9** (50 mg, 0.292 mmol, 1 equiv) in anhydrous THF (4.5 mL/mmol) at −78 °C under argon. After 30 min, the reaction was quenched with satd. NH$_4$Cl (34 mL/mmol). The aqueous layer was then extracted with ethyl acetate (3×7 mL) and washed with water (3×10 mL), followed by brine (2×10 mL). The organic layer was dried over Na$_2$SO$_4$, and evaporated to give **10** as an orange solid. Yield: 54 mg, 94%; M.P.: 119–121 °C; ^{1}H-NMR (500 MHz, CDCl$_3$): δ 7.93 (dd, $J=8.0$, 1.5 Hz, 1H, H9), 7.25 (td, $J=7.8$, 1.4 Hz, 1H, H7), 6.93 (td, $J=7.9$, 1.2 Hz, 1H, H8), 6.83 (d, $J=8.0$ Hz, 1H, H6), 5.18 (qd, $J=6.5$, 3.0 Hz, 1H, CH), 4.23 (s, 1H, NH), 1.75 (dd, $J=6.5$, 3.0 Hz, 3H, CH$_3$); ^{13}C-NMR (125 MHz, CDCl$_3$): δ 150.50 (C3a), 135.20 (C9a), 129.96 (C8), 120.23 (5a), 120.19 (C7), 119.70 (C8), 117.18 (C9), 115.28 (C6), 46.50 (CH), 20.63 (CH$_3$). Spectroscopic data and melting point agree with those reported in the literature.[47]

2-Hydrazino-3-methylquinoxaline (**6**). 2-Chloro-4-methyl quinoxaline (170 mg, 0.957 mmol) and hydrazine monohydrate (238 mg, 4.75 mmol) were dissolved in EtOH (5.2 mL). The reaction mixture was stirred at 50 °C until the starting material could not be detected by TLC (6 h). The solvent was then eliminated under reduced pressure and the residue thus obtained was purified by silica gel column chromatography on silica gel (CH_2Cl_2/CH$_3$OH, 9:1) to give **6** as a red solid. Yield: 164 mg, 99%; ^{1}H-NMR (300 MHz, CDCl$_3$): δ 7.86 (d, $J=8.1$ Hz, 1H, H5), 7.75 (d, $J=8.1$ Hz, 1H, H8), 7.57 (td, $J=8.1$, 1.4 Hz, 1H, H7), 7.43 (td, $J=7.6$, 0.8 Hz, 1H, H6), 6.97 (s, 2H, NH$_2$), 6.14 (s, 1H, NH), 2.55 (s, 3H, CH$_3$). Spectroscopic data agree with those reported in the literature.[47]

1H-Quinoxalin-2-one (**7**). A solution of *o*-phenylenediamine (2.75 g 25 mmol, 1 equiv) and glyoxylic acid (2.2 g, 25 mmol, 1 equiv, 50% wt in water) was refluxed for 2 h. The resulting precipitate was filtered and washed with cold methanol and dried in vacuum to give **7** as a white solid. Yield: 5 g, 97%; ^{1}H-NMR (300 MHz, CDCl$_3$): δ 11.79 (s, 1H, -NH), 8.41 (s, 1H, H3), 7.79 (dd, $J=8.1$, 1.3 Hz, 1H, H5), 7.51 (td, 1H, H7), 7.42–7.25 (m, 2H, H6 and H8), 2.53 (s, 3H, CH$_3$). Spectroscopic data agree with those reported in the literature.[65]

2-Chloroquinoxaline (**8**). A suspension of **7** (1 g, 6.84 mmol) in POCl$_3$ (1.17 ml/mmol) was refluxed at 120 °C for 5 h. The resulting mixture was then cooled to room temperature and poured into a DMF-ice bath. The solid was filtered off, washed with DMF and recrystallized from DMF to yield **8** as a colorless crystalline solid. Yield; 750 mg, 66%; ^{1}H-NMR (300 MHz, CDCl$_3$): δ 8.75 (s, 1H, H3), 8.07 (td, $J=8.0$, 1.8 Hz, 1H, H6), 8.01 (m, H7), 7.81–7.69 (m, 2H, H5 and H8). Spectroscopic data agree with those reported in the literature.[66]

Enzyme inhibition

For IC$_{50}$ and inhibition percentage determination, previously described methods described elsewhere[36] were used. Briefly, Recombinant 322 amino acids PTP1B was purchased from Enzo Life Sciences® while 341 amino acids TCPTP was purchased from Merck. Increasing concentrations of compounds were used to determinate the IC$_{50}$. In each experiment, the hydrolysis of pNPP was measured as an increment in absorbance at 405 nm by adding substrate solution to a solution consisting of inhibitor and enzyme. Each data

ChemMedChem

Full Papers
doi.org/10.1002/cmdc.202100338

Chemistry Europe
European Chemical
Societies Publishing

point was measured by duplicate. Data thus obtained were fitted with GraphPad® (SPCC Inc., Chicago, IL).

Cell culture and differentiation induction

Mouse skeletal muscle cell lines, C2 C12 myoblasts (from ATCCH CRL-1772TM) were cultivated un Dulbecco's modified Eagles medium supplemented with 10% heat-inactivated fetal bovine serum (FBS), 100 U/ml penicillin, 100 U/ml streptomycin at 37 °C in humidified air containing 5% CO2. Differentiation was induced by switching the growth medium to DMEM supplemented with 2% horse serum (HS; differentiation medium). The differentiation medium was changed every 48 h.[67]

Glucose uptake

Glucose uptake was performed as described previously.[36] Briefly, C2 C12 cells cultured in DMEM were treated with compounds **2** and **3** (2 μM, 90 min) or insulin (10 nM, 30 min) before adding 0.1 mM of the fluorescent D-glucose analog 2-[N(7 nitrobenz-2-oxa-1,3-diazol-4)amino]-2-deoxy-glucose (2-NBDG, Sigma-Aldrich). After 30 min incubation, free 2-NBDG was washed out 3 times with cold PBS. Rates of glucose uptake were determined as the intracellular fluorescence (VICTORX4, PerkinElmer), and calculated after subtraction of autofluorescence from negative control without 2-NBDG. Cells were then lysed, the protein content was determined in each experiment with a BCA protein assay kit, and fluorescence values corrected for protein content.

Acknowledgements

Conflict of Interest

The authors declare no conflict of interest.

[1] D. Barford, *Curr. Opin. Struct. Biol.* **1995**, *5*, 728–734.
[2] F. M. Ferguson, N. S. Gray, *Nat. Rev. Drug Discovery* **2018**, *17*, 353–377.
[3] R. M. Crean, M. Biler, M. W. van der Kamp, A. C. Hengge, S. C. L. Kamerlin, *J. Am. Chem. Soc.* **2021**, *143*, 3830–3845.
[4] D. S. Cui, J. M. Lipchock, D. Brookner, J. P. Loria, *J. Am. Chem. Soc.* **2019**, *141*, 12634–12647.
[5] D. A. Keedy, Z. B. Hill, J. T. Biel, E. Kang, T. J. Rettenmaier, J. Brandão-Neto, N. M. Pearce, F. von Delft, J. A. Wells, J. S. Fraser, *eLife* **2018**, *7*, 10.7554/eLife.36307.
[6] N. K. Tonks, C. D. Diltz, E. H. Fischer, *J. Biol. Chem.* **1988**, *263*, 6731–6737.
[7] M. Feldhammer, N. Uetani, D. Miranda-Saavedra, M. L. Tremblay, *Crit. Rev. Biochem. Mol. Biol.* **2013**, *48*, 430–445.
[8] A. J. Hale, E. Ter Steege, J. den Hertog, *Dev. Biol.* **2017**, *428*, 283–292.
[9] S. Nandi, M. Saxena, *Curr. Top. Med. Chem.* **2020**, *20*, 2692–2707.
[10] T. A. Brandão, A. C. Hengge, S. J. Johnson, *J. Biol. Chem.* **2010**, *285*, 15874–15883.
[11] S. Koren, I. G. Fantus, *Best Pract. Res. Clin. Endocrinol. Metab.* **2007**, *21*, 621–640.
[12] M. Elchebly, P. Payette, E. Michaliszyn, W. Cromlish, S. Collins, A. L. Loy, D. Normandin, A. Cheng, J. Himms-Hagen, C. C. Chan, C. Ramachandran, M. J. Gresser, M. L. Tremblay, B. P. Kennedy, *Science* **1999**, *283*, 1544–1548.
[13] S. Zhang, Z. Y. Zhang, *Drug Discovery Today* **2007**, *12*, 373–381.
[14] M. N. Vieira, L. E. Silva, S. T. Ferreira, F. G. De Felice, *Front. Aging Neurosci.* **2017**, *9*, 7.
[15] J. Ghalayini, *J. Neurosci.* **2020**, *40*, 6100–6102.
[16] B. Sharma, L. Xie, F. Yang, W. Wang, Q. Zhou, M. Xiang, S. Zhou, W. Lv, Y. Jia, L. Pokhrel, J. Shen, Q. Xiao, L. Gao, W. Deng, *Eur. J. Med. Chem.* **2020**, *199*, 112376.
[17] B. T. Zhao, D. H. Nguyen, D. D. Le, J. S. Choi, B. S. Min, M. H. Woo, *Arch. Pharmacal Res.* **2018**, *41*, 130–161.
[18] Z. Y. Zhang, S. Y. Lee, *Expert Opin. Invest. Drugs* **2003**, *12*, 223–233.
[19] G. S. Kumar, R. Page, W. Peti, *PLoS One* **2020**, *15*, e0240044.
[20] S. Fukuda, T. Ohta, S. Sakata, H. Morinaga, M. Ito, Y. Nakagawa, M. Tanaka, M. Matsushita, *Diabetes Obes. Metab.* **2010**, *12*, 299–306.
[21] C. Wiesmann, K. J. Barr, J. Kung, J. Zhu, D. A. Erlanson, W. Shen, B. J. Fahr, M. Zhong, L. Taylor, M. Randal, R. S. McDowell, S. K. Hansen, *Nat. Struct. Mol. Biol.* **2004**, *11*, 730–737.
[22] A. P. Combs, W. Zhu, M. L. Crawley, B. Glass, P. Polam, R. B. Sparks, D. Modi, A. Takvorian, E. McLaughlin, E. W. Yue, Z. Wasserman, M. Bower, M. Wei, M. Rupar, P. J. Ala, B. M. Reid, D. Ellis, L. Gonneville, T. Emm, N. Taylor, S. Yeleswaram, Y. Li, R. Wynn, T. C. Burn, G. Hollis, P. C. Liu, B. Metcalf, *J. Med. Chem.* **2006**, *49*, 3774–3789.
[23] T. O. Johnson, J. Ermolieff, M. R. Jirousek, *Nat. Rev. Drug Discovery* **2002**, *1*, 696–709.
[24] K. Varshney, S. Gupta, N. Rahuja, A. K. Rawat, N. Singh, A. K. Tamarkar, A. K. Srivastava, A. K. Saxena, *ChemMedChem* **2012**, *7*, 1185–1190.
[25] H. Hussain, I. R. Green, G. Abbas, S. M. Adekenov, W. Hussain, I. Ali, *Expert Opin. Ther. Pat.* **2019**, *29*, 689–702.
[26] V. M. Balaramnavar, R. Srivastava, S. Varshney, S. Kumar, A. K. Rawat, H. Chandasana, Y. S. Chhonker, R. S. Bhatta, A. K. Srivastava, A. N. Gaikwad, V. Lakshmi, A. K. Saxena, *Bioorg. Chem.* **2021**, *110*, 104829.
[27] X. F. He, J. J. Chen, T. Z. Li, J. Hu, X. M. Zhang, C. A. Geng, *Bioorg. Chem.* **2021**, *108*, 104683.
[28] G. Schneider, W. Neidhart, T. Giller, G. Schmid, *Angew. Chem. Int. Ed. Engl.* **1999**, *38*, 2894–2896.
[29] Y. Hu, D. Stumpfe, J. Bajorath, *J. Med. Chem.* **2017**, *60*, 1238–1246.
[30] F. Grisoni, G. Schneider, *Methods Mol. Biol.* **2021**, *2266*, 11–35.
[31] J. Z. Liu, S. E. Zhang, F. Nie, Y. Yang, Y. B. Tang, W. Yin, J. Y. Tian, F. Ye, Z. Xiao, *Bioorg. Med. Chem. Lett.* **2013**, *23*, 6217–6222.
[32] V. M. Balaramnavar, R. Srivastava, N. Rahuja, S. Gupta, A. K. Rawat, S. Varshney, H. Chandasana, Y. S. Chhonker, P. K. Doharey, S. Kumar, S. Gautam, S. P. Srivastava, R. S. Bhatta, J. K. Saxena, A. N. Gaikwad, A. K. Srivastava, A. K. Saxena, *Eur. J. Med. Chem.* **2014**, *87*, 578–594.
[33] W. L. Wang, X. Y. Chen, Y. Gao, L. X. Gao, L. Sheng, J. Zhu, L. Xu, Z. Z. Ding, C. Zhang, J. Y. Li, J. Li, Y. B. Zhou, *Bioorg. Med. Chem. Lett.* **2017**, *27*, 5154–5157.
[34] R. N. Shinde, G. S. Kumar, S. Eqbal, M. E. Sobhia, *PLoS One* **2018**, *13*, e0199020.
[35] M. De Vivo, M. Masetti, G. Bottegoni, A. Cavalli, *J. Med. Chem.* **2016**, *59*, 4035–4061.
[36] J. García-Marín, M. Griera, P. Sánchez-Alonso, B. Di Geronimo, F. Mendicuti, M. Rodríguez-Puyol, R. Alajarín, B. de Pascual-Teresa, J. J. Vaquero, D. Rodríguez-Puyol, *ChemMedChem* **2020**, *15*, 1788–1801.
[37] P. R. Lazzara, T. W. Moore, *RSC Med. Chem.* **2020**, *11*, 18–29.
[38] L. D. Pennington, D. T. Moustakas, *J. Med. Chem.* **2017**, *60*, 3552–3579.
[39] W. Jespers, J. Åqvist, H. Gutiérrez-de-Terán, *Methods Mol. Biol.* **2021**, *2266*, 203–226.
[40] Z. Cournia, B. Allen, W. Sherman, *J. Chem. Inf. Model.* **2017**, *57*, 2911–2937.
[41] G. M. Javier, *J. Biomol. Struct. Dyn.* **2020**, 1–12.
[42] S. C. Kamerlin, R. Rucker, S. Boresch, *Biochem. Biophys. Res. Commun.* **2007**, *356*, 1011–1016.
[43] R. N. Shinde, M. E. Sobhia, *J. Mol. Graphics Modell.* **2013**, *45*, 98–110.
[44] T. Jin, H. Yu, X. F. Huang, *Sci. Rep.* **2016**, *6*, 20766.

ChemMedChem

Full Papers
doi.org/10.1002/cmdc.202100338

**Chemistry
Europe**
European Chemical
Societies Publishing

[45] S. Li, J. Zhang, S. Lu, W. Huang, L. Geng, Q. Shen, J. Zhang, *PLoS One* **2014**, *9*, e97668.

[46] S. Wagle, A. V. Adhikari, N. S. Kumari, *Eur. J. Med. Chem.* **2009**, *44*, 1135–1143.

[47] A. L. Chandgude, A. Dömling, *Eur. J. Org. Chem.* **2016**, *2016*, 2383–2387.

[48] L. F. Iversen, K. B. Moller, A. K. Pedersen, G. H. Peters, A. S. Petersen, H. S. Andersen, S. Branner, S. B. Mortensen, N. P. Moller, *J. Biol. Chem.* **2002**, *277*, 19982–19990.

[49] A. J. Barr, *Future Med. Chem.* **2010**, *2*, 1563–1576.

[50] P. Virtanen, R. Gommers, T. E. Oliphant, M. Haberland, T. Reddy, D. Cournapeau, E. Burovski, P. Peterson, W. Weckesser, J. Bright, S. J. van der Walt, M. Brett, J. Wilson, K. J. Millman, N. Mayorov, A. R. J. Nelson, E. Jones, R. Kern, E. Larson, C. J. Carey, İ Polat, Y. Feng, E. W. Moore, J. VanderPlas, D. Laxalde, J. Perktold, R. Cimrman, I. Henriksen, E. A. Quintero, C. R. Harris, A. M. Archibald, A. H. Ribeiro, F. Pedregosa, P. van Mulbregt, *Nat. Methods* **2020**, *17*, 352–5; Polat, Y. Feng, E. W. Moore, J. VanderPlas, D. Laxalde, J. Perktold, R. Cimrman, I. Henriksen, E. A. Quintero, C. R. Harris, A. M. Archibald, A. H. Ribeiro, F. Pedregosa, P. van Mulbregt, *Nat. Methods* **2020**, *17*, 352–5.

[51] J. A. Maier, C. Martinez, K. Kasavajhala, L. Wickstrom, K. E. Hauser, C. Simmerling, *J. Chem. Theory Comput.* **2015**, *11*, 3696–3713.

[52] J. Wang, R. M. Wolf, J. W. Caldwell, P. A. Kollman, D. A. Case, *J. Comput. Chem.* **2004**, *25*, 1157–1174.

[53] X. He, V. H. Man, W. Yang, T. S. Lee, J. Wang, *J. Chem. Phys.* **2020**, *153*, 114502.

[54] J. Wang, W. Wang, P. A. Kollman, D. A. Case, *J. Mol. Graphics Modell.* **2006**, *25*, 247–260.

[55] R. Salomon-Ferrer, D. A. Case, R. C. Walker, *WIREs Comput. Mol. Sci.* **2013**, *3*, 198–210.

[56] P. Eastman, J. Swails, J. D. Chodera, R. T. McGibbon, Y. Zhao, K. A. Beauchamp, L. P. Wang, A. C. Simmonett, M. P. Harrigan, C. D. Stern, R. P. Wiewiora, B. R. Brooks, V. S. Pande, *PLoS Comput. Biol.* **2017**, *13*, e1005659.

[57] J. Klett, A. Núñez-Salgado, H. G. Dos Santos, Á Cortés-Cabrera, A. Perona, R. Gil-Redondo, D. Abia, F. Gago, A. Morreale, *J. Chem. Theory Comput.*

[58] R. T. McGibbon, K. A. Beauchamp, M. P. Harrigan, C. Klein, J. M. Swails, C. X. Hernández, C. R. Schwantes, L. P. Wang, T. J. Lane, V. S. Pande, *Biophys. J.* **2015**, *109*, 1528–1532.

[59] N. Michaud-Agrawal, E. J. Denning, T. B. Woolf, O. Beckstein, *J. Comput. Chem.* **2011**, *32*, 2319–2327.

[60] J. Reback, W. McKinney, jbrockmendel, J. V.d. Bossche, T. Augspurger, P. Cloud, gfyoung, Sinhrks, A. Klein, M. Roeschke, J. Tratner, C. She, W. Ayd, S. Hawkins, T. Petersen, J. Schendel, A. Hayden, M. Garcia, V. Jancauskas, MomIsBestFriend, P. Battiston, S. Seabold, chris-b1, h-vetinari, S. Hoyer, W. Overmeire, M. Mehyar, C. Whelan, T. Kluyver, **2020**.

[61] T. A. Caswell, M. Droettboom, A. Lee, E. S.d. Andrade, J. Hunter, T. Hoffmann, E. Firing, J. Klymak, D. Stansby, N. Varoquaux, J. H. Nielsen, B. Root, R. May, P. Elson, J. K. Seppänen, D. Dale, J. Lee, D. McDougall, A. Straw, P. Hobson, C. Gohlke, T. S. Yu, E. Ma, A. F. Vincent, S. Silvester, C. Moad, N. Kniazev, E. Ernest, P. Ivanov, **2021** *Zenodo*, matplotlib/matplotlib.

[62] M. Waskom, **2021** *Zenodo*. seaborn: v0.7.1 (June 2016).

[63] W. Humphrey, A. Dalke, K. Schulten, *J. Mol. Graphics* **1996**, *14*, 33–8.

[64] E. F. Pettersen, T. D. Goddard, C. C. Huang, E. C. Meng, G. S. Couch, T. I. Croll, J. H. Morris, T. E. Ferrin, *Protein Sci.* **2021**, *30*, 70–82.

[65] G. M. Fischer, M. Isomäki-Krondahl, I. Göttker-Schnetmann, E. Daltrozzo, A. Zumbusch, *Chemistry* **2009**, *15*, 4857–4864.

[66] M. N. Noolvi, H. M. Patel, V. Bhardwaj, A. Chauhan, *Eur. J. Med. Chem.* **2011**, *46*, 2327–2346.

[67] J. S. Chang, I. D. Kong, *Pfluegers Arch.* **2020**, *472*, 495–502.